The Astrophysical Journal Letters, 769:L15 (6pp), 2013 May 20 doi:10.1088/2041-8205/769/1/L15

THE MAGNETIC FIELD MORPHOLOGY OF THE CLASS 0 PROTOSTAR L1157-mm

Ian W. Stephens[1], Leslie W. Looney[1,2], Woojin Kwon[1,3], Charles L. H. Hull[4], Richard L. Plambeck[4], Richard M. Crutcher[1], Nicholas Chapman[5], Giles Novak[5], Jacqueline Davidson[6], John E. Vaillancourt[7], Hiroko Shinnaga[8], and Tristan Matthews[5]
[1] Department of Astronomy, University of Illinois, 1002 West Green Street, Urbana, IL 61801, USA; stephen6@illinois.edu
[2] National Radio Astronomy Observatory, 520 Edgemont Road, Charlottesville, VA 22903, USA
[3] SRON Netherlands Institute for Space Research, Landleven 12, 9747 AD Groningen, The Netherlands
[4] Astronomy Department and Radio Astronomy Laboratory, 601 Campbell Hall, University of California, Berkeley, CA 94720, USA
[5] Center for Interdisciplinary Exploration and Research in Astrophysics (CIERA) & Department of Physics & Astronomy, Northwestern University, 2145 Sheridan Road, Evanston, IL 60208, USA
[6] School of Physics, University of Western Australia, 35 Stirling Hwy, Crawley, WA 6009, Australia
[7] SOFIA Science Center, Universities Space Research Association, NASA Ames Research Center, MS 232-11, Moffett Field, CA 94035-0001, USA
[8] Subaru Telescope, National Astronomical Observatory of Japan, 650 North A'ohoku Place, Hilo, HI 96720, USA
Received 2013 March 16; accepted 2013 April 23; published 2013 May 7

ABSTRACT

We present the first detection of polarization around the Class 0 low-mass protostar L1157-mm at two different wavelengths. We show polarimetric maps at large scales (10″ resolution at 350 μm) from the SHARC-II Polarimeter and at smaller scales (1.″2–4.″5 at 1.3 mm) from the Combined Array for Research in Millimeter-wave Astronomy (CARMA). The observations are consistent with each other and show inferred magnetic field lines aligned with the outflow. The CARMA observations suggest a full hourglass magnetic field morphology centered about the core; this is only the second well-defined hourglass detected around a low-mass protostar to date. We apply two different methods to CARMA polarimetric observations to estimate the plane-of-sky magnetic field magnitude, finding values of 1.4 and 3.4 mG.

Key words: galaxies: star formation – magnetic fields – polarization – stars: protostars

Online-only material: color figures

1. INTRODUCTION

Alignment of dust grains by magnetic fields causes the thermal emission from dust to be polarized (e.g., Hildebrand 1988). The angles of dust polarization measurements at millimeter and submillimeter wavelengths are generally considered to be perpendicular to the magnetic field due to a number of alignment mechanisms (particularly radiative torques; Lazarian 2007), allowing for an estimate of the magnetic field direction in the plane of the sky.

Magnetic pressure can support clouds against collapse, though other processes, e.g., ambipolar diffusion, can allow gravity to eventually overwhelm magnetic support. The importance of magnetic fields in star formation is not well understood (e.g., weak- versus strong-field models; Crutcher 2012), but observations of the plane-of-sky magnetic field morphology can provide insight into the coupling of magnetic fields with cores, disks, and outflows. Although flux-freezing during gravitational collapse is expected to create an hourglass morphology in the magnetic field lines, there has only been one detection of a full hourglass around a low-mass protostar to date (e.g., Girart et al. 2006). However, several high-mass star formation regions have clear hourglass detections (e.g., Schleuning 1998; Girart et al. 2009; Tang et al. 2009).

Large, submillimeter surveys of various star-forming clouds and cores have been performed with single-dish polarimeters (e.g., Matthews et al. 2009; Dotson et al. 2010). The SHARC-II Polarimeter (SHARP; Li et al. 2008) at the Caltech Submillimeter Observatory, is one of the newer submillimeter polarimeters and allows for dual-beam (simultaneous observations of horizontal and vertical polarization components) polarimetric measurements.

Previous millimeter-wavelength interferometric polarimetric maps have been produced with the Berkeley–Illinois–Maryland Association, the Owens Valley Radio Observatory, and the Submillimeter Array (SMA) (e.g., Girart et al. 2006; Kwon et al. 2006; Rao et al. 2009; Tang et al. 2010), but these observations only used single-polarization receivers modulated with a quarter-wave plate. The Combined Array for Research in Millimeter-wave Astronomy (CARMA) has recently installed 1 mm dual-polarization receivers; the first science observations in full-Stokes were made in 2011.

In this Letter we present polarimetric observations from SHARP and CARMA of the protostar L1157-mm in the dark cloud L1157. L1157-mm is a low-mass Class 0 source (i.e., the youngest of protostars) with a large bipolar outflow spanning about 5′ (Bachiller et al. 2001) and a perpendicular 2′ flattened envelope (Looney et al. 2007). Though the distance to the source is a bit uncertain, with estimates ranging from 200 to 450 pc (e.g., Kun 1998), we adopt a distance of 250 pc (Looney et al. 2007).

These observations trace the magnetic field structure within the core and throughout the infall envelope (which, given the adopted distance, could extend to 30″–40″) of L1157-mm. In this Letter we will examine how the continuum and the magnetic field morphologies correlate with other structures in L1157, such as its outflow and flattened core, and will estimate the field strength.

2. OBSERVATIONS AND DATA REDUCTION

With SHARP and CARMA we create polarimetric maps that show the fractional linear polarization, $P = \sqrt{Q^2 + U^2}/I$ (where I, Q, and U are Stokes parameters) and the angle with

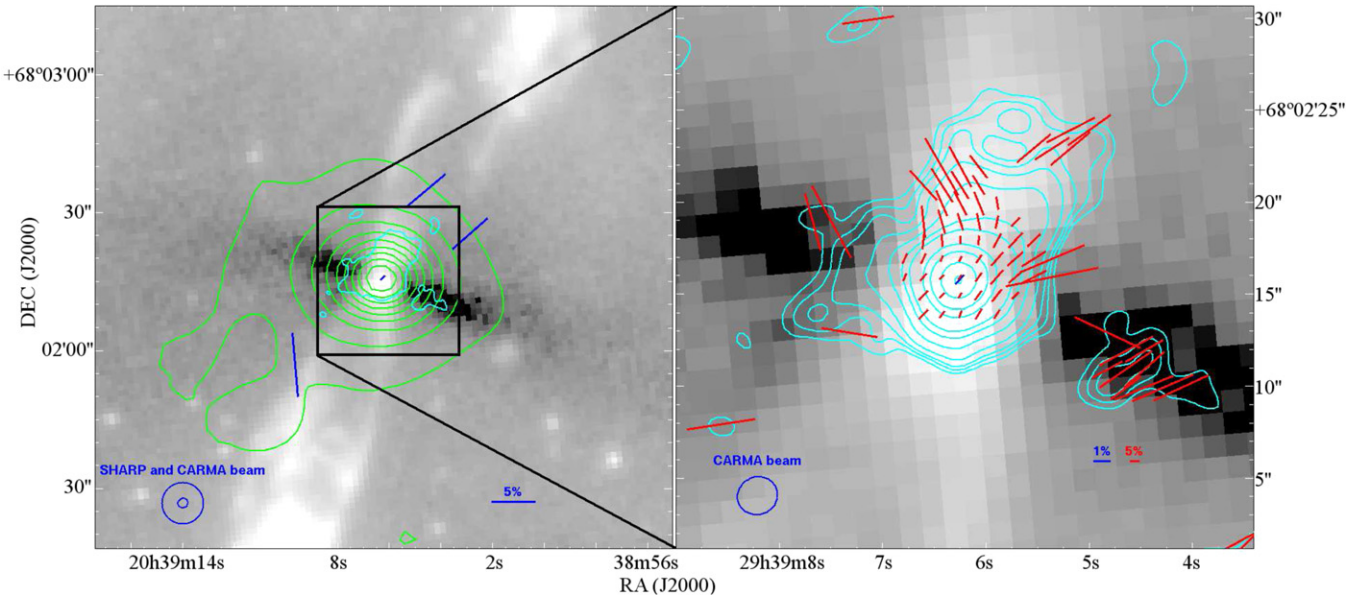

Figure 1. Polarimetric maps (with polarization vectors rotated by 90° to show the inferred magnetic field orientation) of L1157-mm with the grayscale background showing a log-scale map of *Spitzer* 8 μm emission (Looney et al. 2007). Magnetic field vectors are shown for $P_I > 2\sigma_{P_I}$ and $I > 2\sigma_I$. Left: SHARP continuum contours and vectors are shown in green and blue respectively. Cyan shows the 2σ intensity detections from CARMA. The length of the vectors is proportional to P. SHARP contour levels range from 10% to 90% in 10% increments of the peak flux. Right: cyan (red) contours (vectors) are the combined CARMA data at 2.″1 resolution and the central blue vector is from SHARP. CARMA contour levels are [2, 3, 4, 6, 10, 15, 20, 40, 60, 100, 140] $\times\sigma$, $\sigma = 1.02$ mJy beam^{-1}. Negative contours are not shown.

(A color version of this figure is available in the online journal.)

respect to the plane of the sky, θ (measured counterclockwise from north). When making uncertainty cuts based on polarization, we used polarized intensity, $P_I = I\,P$ rather than P. Due to the only positive nature of P and P_I, de-biasing these values is necessary (e.g., Vaillancourt 2006) and was done for all observations.

2.1. SHARP

Polarimetric observations of L1157-mm were made with SHARP in 2008 September. These observations were at 350 μm (resolution of $\sim$10″) and were mosaicked in a chop/nod observing mode. The SHARP data reduction is discussed in Chapman et al. (2013). The total integration time on L1157 is about 15.8 hr; due to constant chopping, the integration time on the source is closer to 7 hr.

2.2. CARMA

CARMA observations of L1157 in full-Stokes mode at 1.3 mm were first made in the E-array ($\sim$4.″6 resolution) in 2011 July as a CARMA summer school project. Additional observations in the D- ($\sim$2″) and C- ($\sim$0.″8) arrays were obtained over the next year as part of the TADPOL (Telescope Array Doing POLarization) key project (e.g., Hull et al. 2013). An additional D-array summer school observation was also added in 2012 June.

The CARMA dual-polarization system is capable of measuring all four cross-correlations simultaneously through the circularly polarized feeds and full-Stokes correlator. The reduction process for the data in this Letter is explained in Hull et al. (2013). For L1157-mm, the flux calibrator was typically MWC349, but when this source was unavailable, we used Mars or Neptune. Flux calibration is accurate within $\sim$15%; however, for the rest of the Letter, only statistical uncertainties are discussed. The phase calibrator used for all tracks was 1927+739.

3. RESULTS

Figure 1 shows the results (dust continuum and the inferred magnetic field orientation) for SHARP and the combined CARMA observations. In the 350 μm SHARP map, an extension of the continuum is seen toward the southeast with a positional angle (PA, measured counterclockwise from north) of about 124°, differing from the PA of the outflow of 161° (Bachiller et al. 2001); however, this extension roughly coincides with N_2H^+ extension seen in Chiang et al. (2010). In the combined CARMA data, the continuum is extended toward the northwest with PA $\approx -20°$, which agrees well with $\sim -27°$ from *Spitzer* 8 μm and with $-19°$ from Bachiller et al. (2001). This extension may be due to photons preferentially escaping through the poles, thus heating the outflow cavity. The continuum also extends toward the east, showing the flattened envelope of L1157-mm; this extension matches very well with *Spitzer* and N_2H^+ observations of the flattened structure (Chiang et al. 2010). Additionally, the continuum observations show an indication of this flattened structure toward the west. The east and west continuum extensions are also seen at 1.3 mm with the SMA at $\sim$5.″5 resolution (Tobin et al. 2013).

For SHARP, all vectors are aligned within $\sim$30° with the outflow angle measured by Bachiller et al. (2001); however, the southeast vector is offset from the mean of the other three vectors by 50°. CARMA vectors have a definitive hourglass shape, with the hourglass axis nearly coinciding with that of the outflow (Figure 2). We note that the difference between the hourglass axis and the outflow axis (a proxy for rotation axis) is about 15°.[9] We do not discuss the reason for this discrepancy, though we note that W. Kwon et al. (in preparation) discusses

[9] Hull et al. (2013) derived a PA difference of 0° for L1157 because they defined the outflow direction as the line connecting the two brightest CO(2–1) peaks, whereas we follow Bachiller et al. (2001), which uses the midline of the outflow cones.

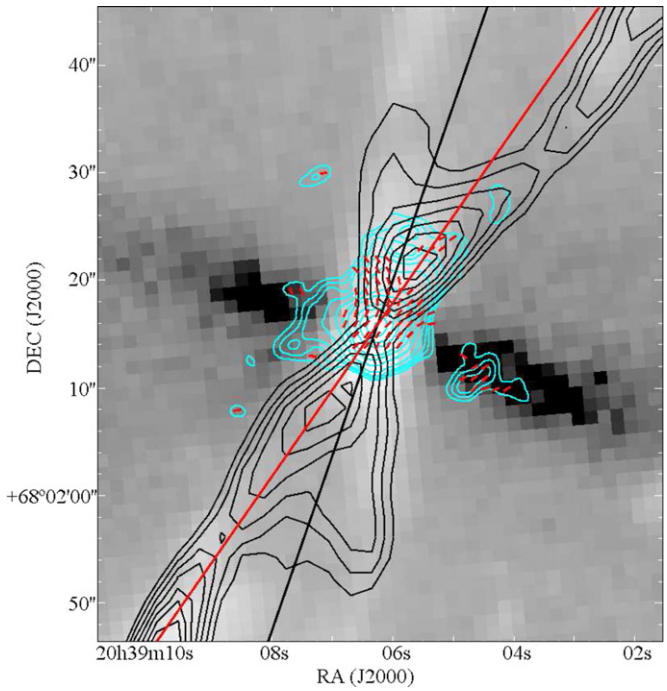

Figure 2. Hourglass morphology of L1157 with the red line showing the axis of the hourglass and the black line showing the center of the outflow from Bachiller et al. (2001). Cyan and red vectors are the same as Figure 1. Black contours show the CO(2–1) moment-0 map (integrated intensity) of the outflow with contour levels of [2, 3, 4, 5, 6, 7, 8, 9] × σ, σ = 8 Jy beam^{-1} km s^{-1} (W. Kwon et al., in preparation). Negative contours are not shown.

(A color version of this figure is available in the online journal.)

the possibility of two jets ejected from L1157-mm, and our hourglass is tilted toward the more CO-bright (and probably more massive) jet. We note that the northwest SHARP vectors also coincides better with the CO-bright jet (within ∼15°) than the entire outflow (within ∼30°).

As seen in Figure 1, we also find that for both CARMA and SHARP observations, P is significantly less toward the center of the object, which is typical in polarimetric observations (e.g., Girart et al. 2006). Several factors may contribute to lower central fractional polarization, such as: (1) averaging along the line of sight is more likely to smear out the polarization through the thickest part of the source, (2) de-polarization at higher density, and (3) different grain populations at the center.

3.1. Comparison between Different Wavelengths

To compare SHARP and CARMA values, we smooth the CARMA data to a beam size of 10″ to provide accurate comparison between wavelengths. We find that the central vectors have $P = 0.7\% \pm 0.2\%$, $\theta = -37.^{\circ}9 \pm 9.^{\circ}0$ for SHARP and $P = 3.80\% \pm 0.11\%$, $\theta = -32.^{\circ}2 \pm 0.^{\circ}8$ for the CARMA data. These vectors are our only point of comparison, and the angles are consistent with each other. This central angle is also consistent at all CARMA resolutions (see Figure 3).

Studies have attempted to explain polarization spectra observed in various molecular clouds. Vaillancourt & Matthews (2012) present $P[\lambda]/P[350]$ values at wavelengths, λ, of 60, 100, 850, and 1300 μm. The median $P[\lambda]/P[350]$ value of a cloud can vary dramatically, but the typical value for these wavelengths was ∼2. Our value of $P[1300]/P[350] \approx 5.4$ does not fit well within this polarization spectrum. However, comparisons of single dish and interferometric fractional polarization should be made with caution; e.g., with varying polarization across the source, the interferometer tends to resolve out Stokes I more than Stokes Q or U, causing P to be overestimated. Additionally, we only have one point of comparison.

3.2. Comparison between Different Size Scales

When a cloud with initially parallel magnetic field lines collapses and flux-freezing holds at least partially, the field becomes pinched into an hourglass morphology. According to ambipolar diffusion low-mass star formation models (e.g., Fiedler & Mouschovias 1993; Galli & Shu 1993; Allen et al. 2003), the hourglass size may range from the size of the protostar cloud core (a few hundred to a few thousand AU) to the size of the protostar infall envelope (up to about 10,000 AU). Our observations probe resolutions from ∼300–2250 AU and will provide a diagnostic of the size scale of the pinch.

From our combined CARMA observations, we apply three different Gaussian tapers to the visibility data which, along with the non-tapered data, probe four different resolutions (1.″2, 2.″1, 3.″0, and 4.″5) as seen in Figure 3. We note that L1157-mm is only marginally resolved at 4.″5 resolution. Red vectors are shown when $P_I > 2\sigma_{P_I}$ and are shown spatially at approximately Nyquist frequency (∼2 vectors per beam). In attempt to see the most morphology possible given our sensitivity, we also show yellow vectors for $1.5\sigma_{P_I} < P_I < 2\sigma_{P_I}$.[10]

Parts of the hourglass morphology can be detected in the lower resolution maps, but the full hourglass becomes evident in the two higher resolution plots. SHARP data, however, fail to see a definitive pinch even when considering lower σ detections (the entire low-σ SHARP polarization field is not shown in this Letter).

The resolution at which the *full* hourglass morphology becomes apparent at 1.3 mm is approximately 2.″1 or 550 AU. We note that this size-scale is highly uncertain (particularly due to distance and signal to noise), though it is roughly consistent with the 290 AU resolution probing the hourglass in Girart et al. (2006), assuming a distance to NGC 1333 of 235 pc (Loinard 2013).

3.3. Magnetic Field Strength

The strength of the magnetic field cannot be measured directly from dust polarization maps; however, different methods allow for estimations. The standard technique for calculating magnetic fields from polarimetric maps is the Chandrasekhar–Fermi (CF) technique (Chandrasekhar & Fermi 1953) and modifications of the method.

We use a modified CF technique (Ostriker et al. 2001) in the large central region where polarimetric observations exist ($P_I > 2\sigma_{P_I}$ and $I > 2\sigma_I$ for the combined data at 2.″1 resolution). Our application of the technique follows the methodology outlined in Girart et al. (2006), which fits parabolas to the vectors and uses the residuals from the fits to calculate the angle dispersion in NGC 1333 IRAS 4A.

The central region of L1157-mm has a total flux of 0.35 Jy in an area of 70 arcsec^2. Using a dust temperature of 25 K (H.-F. Chiang 2013, private communication) and a dust opacity of $\kappa_\nu = 0.9$ cm^2 g^{-1} (Ossenkopf & Henning 1994), we find that the central region has a mean volume density of $n(H_2) = 7.4 \times 10^6$ cm^{-3}. From N_2H^+ observations, we use a non-thermal rms

[10] When plotting vectors even down to $P_I/\sigma_{P_I} = 1$, we notice that the scatter from the morphology is typically small ($\lesssim 10^{\circ}$, indicating we have overestimated errors and/or vectors are not independent). Therefore, $1.5\sigma_{P_I}$ vectors help in displaying the magnetic field morphology.

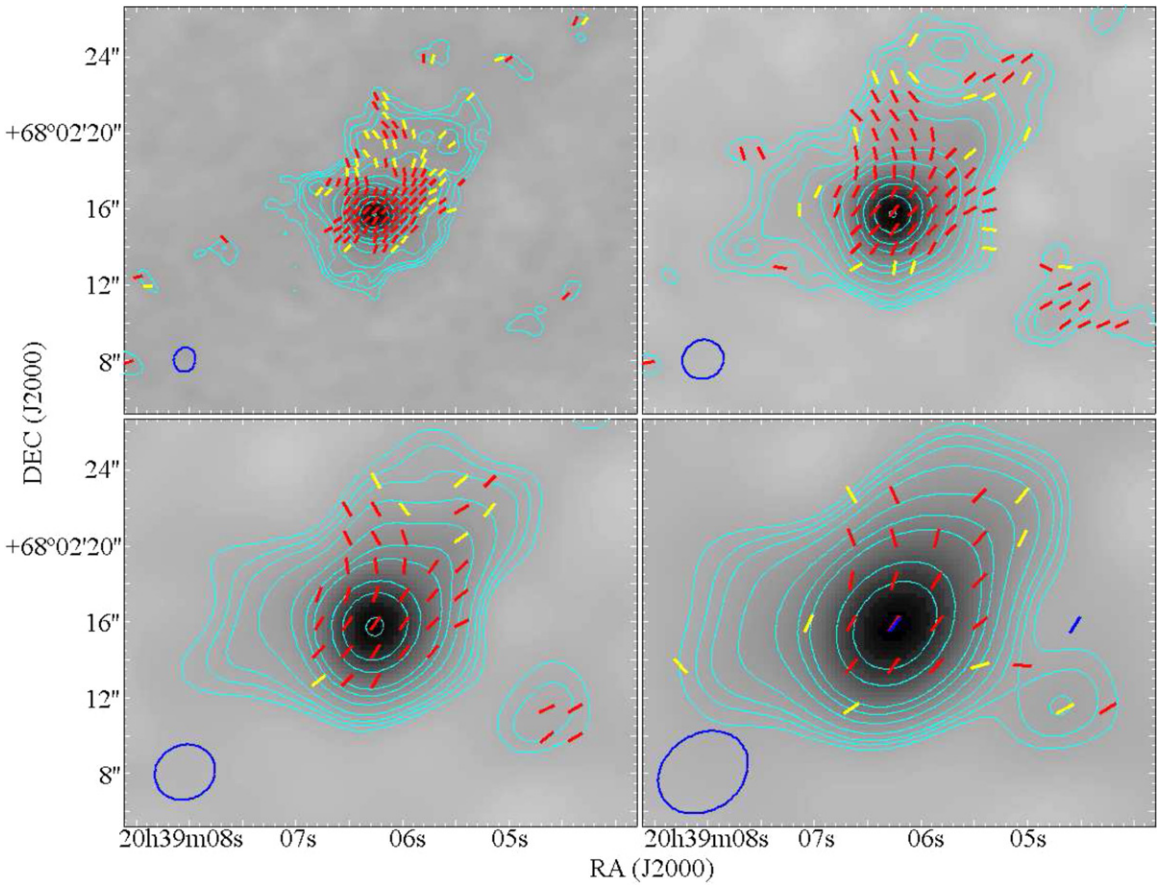

Figure 3. The dust continuum emission and magnetic field morphology as measured by CARMA to determine the size-scale at which we see the hourglass. Gray scale is the Stokes *I* intensity on a square root scale and the blue ellipses show the beam size for each resolution. All vectors have $I > 2\sigma_I$, the red vectors have $P_I > 2\sigma_{P_I}$, and the yellow vectors have $1.5\sigma_{P_I} < P_I < 2\sigma_{P_I}$. Top left: 1.″2 resolution, top right: 2.″1 resolution, bottom left: 3.″0 resolution, and bottom right: 4.″5 resolution, with SHARP vectors for $P_I > 1.5\sigma_{P_I}$ in blue (9″ resolution). The hourglass pinch becomes the most obvious at higher resolution. CARMA contour levels are the same as in Figure 1. The rms error, σ, for each of the four panels is 0.94, 1.02, 1.79, and 2.58 mJy beam^{-1} respectively.

(A color version of this figure is available in the online journal.)

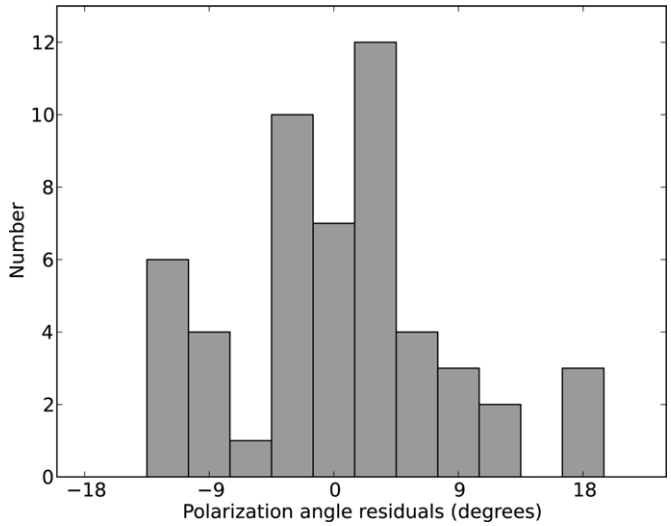

Figure 4. Histogram of angle residuals (difference between measured angle and parabolic fit) at each vector location. One vector in the west of L1157-mm was excluded from the fitting since it caused a large reduced χ^2 value.

velocity dispersion about the line of sight of $\delta v_{\rm los} = 0.18$ km s^{-1} (Chiang et al. 2010). The dispersion from the residuals of parabola fits was 7.°5 (see Figure 4) and the uncertainty of the polarization angle is $\sim 4°$, resulting in an angular dispersion of $\delta\phi = 6°$. Given these parameters, we find a plane-of-sky magnetic field measurement of 1.4 mG. Using these values, the mass-to-magnetic flux ratio (using the method discussed in Crutcher 1999) is found to be 1.1 times the critical value for collapse.

Since the CF method only calculates the average magnetic field strength and has numerous uncertainties (see discussion in Crutcher 2012), we also use another method by Koch et al. (2012) that calculates the magnetic field strength at all locations where there are dust polarization and emission measurements. This technique assumes ideal magnetohydrodynamics (MHD) and that the dust emission gradient indicates the direction of the MHD force equation, leading to the equation for the magnetic field strength below:

$$B = \sqrt{\frac{\sin\psi}{\sin\alpha}(\nabla P + \rho\nabla\phi)4\pi R}. \quad (1)$$

In this equation, ψ is the angle difference between gravity and the intensity gradient, α is the difference between polarization and the intensity gradient, P is the hydrostatic pressure, ϕ is the gravitational potential as a function of radius, and R is the local curvature radius of the polarization vectors. When applying this technique, we assume a density profile of the envelope to follow the fits of L1157-mm observations in Chiang et al. (2012; power-law of $\rho \propto r^{-p}$ with $p = 2$). We also use a central core mass

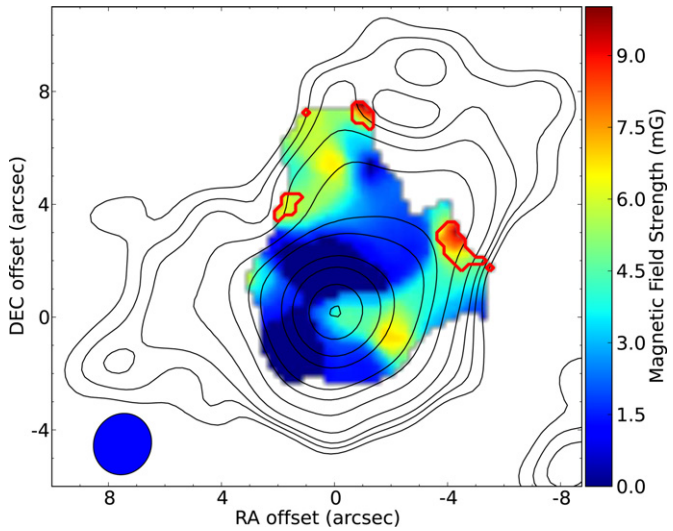

Figure 5. Magnetic field throughout L1157-mm with the color scale in mG. Black contours are the same as Figure 1. Red contours indicate subcritical locations, while the rest of the colored area is supercritical.

(A color version of this figure is available in the online journal.)

of $M_0 = 0.19\ M_\odot$ (assumed to be similar to L1527; Tobin et al. 2012). Additionally, we assume the pressure gradient, ∇P, to be negligible compared to gravity. The local curvature is calculated in the manner suggested in Koch et al. (2012).

The magnetic field throughout the large central region where polarimetric observations exist ($P_I > 2\sigma_{P_I}$ and $I > 2\sigma_I$ for the combined data at 2.″1 resolution) can be seen in Figure 5; outside this area, magnetic field measurements are unreliable. This figure uses median-filtered smoothing at approximately Nyquist sampling (i.e., with pixel sizes of 0.″25, we replace each pixel value by the median of the surrounding 5 × 5 box). The color bar indicates the field strength in mG, with an average and median magnetic field throughout the region of 3.6 and 3.4 mG respectively. The red contours show the locations where magnetic field tension dominates gravity (subcritical). Note that the central areas are supercritical (gravity dominates the magnetic field tension). The Koch et al. (2012) method determines the criticality based on $\sin\psi/\sin\alpha$, while the critical values for the CF method is an average about the entire region and depends on calculated values (e.g., magnetic field strength, mass).

When using the method from Koch et al. (2012) to estimate the magnetic field, we have three free parameters: p, M_0, and distance, d. In the parameter space of our uncertainty in variables, $1.5 < p < 2.5$, $0.1\ M_\odot < M_0 < 0.75\ M_\odot$, and 200 pc $< d <$ 500 pc, the median magnetic field follows the approximate relationship

$$B = 3.4\ \mathrm{mG}\left(\frac{p}{2}\right)^{1.9}\left(\frac{M_0}{0.19\ M_\odot}\right)^{0.5}\left(\frac{d}{250\ \mathrm{pc}}\right)^{0.5}. \quad (2)$$

When altering these parameters, our median magnetic field value of 3.4 mG does not drastically change and will generally be within a factor of ∼2. Note that changing these parameters does not change the supercritical and subcritical locations in the cloud since these locations only depend on the value of $\sin\psi/\sin\alpha$.

4. DISCUSSION

In this Letter we present the first detection of magnetic fields in L1157-mm at two different wavelengths. Our main results are:

1. We find the second instance of a full hourglass morphology in the inferred magnetic field around a low-mass protostar. This is also only the second instance around a Class 0 source. The axis of the hourglass is nearly aligned with the axis of the outflow, with the full detection of the hourglass occurring at a resolution of ∼550 AU.
2. The angle of the central magnetic field vector agrees at 350 μm and 1.3 mm and at all size scales.
3. We used two methods to calculate the plane-of-sky magnetic field throughout the central region and find values of 1.4 and 3.4 mG.

While this particular hourglass is nearly aligned with the outflow, the TADPOL survey results have shown that in general, magnetic field lines are consistent with being preferentially misaligned (perpendicular) or randomly aligned with respect to outflows (Hull et al. 2013).

The first well-defined hourglass morphology around a low-mass protostar was observed in 1997 in the Class 0 binary system NGC 1333 IRAS 4A (Girart et al. 1999); such a discovery has not been published since. Our observation of L1157-mm is arguably the best example of an hourglass shape in any star formation region to date. Characterizing such systems is an important step to better understand the role of magnetic fields in star formation.

IRAS 4A's hourglass axis of symmetry is misaligned with large scale outflow as measured by CO(3–2) (Blake et al. 1995) by 16° and is over 40° misaligned with the small scale outflow as measured by SiO(1–0) (Choi 2005). However, SHARP observations found that the large scale field in IRAS 4A coincides within 1° of the large scale outflow (Attard et al. 2009). Our observations of L1157-mm find that the hourglass axis of symmetry and northwest SHARP vectors are similarly misaligned by ∼15°–30°, but the hourglass axis is more aligned with the outflow than these SHARP vectors. These results suggest the need to compare more polarimetric observations at different resolutions, which will be a future TADPOL project.

Recent high resolution Expanded Very Large Array observations detect only a single continuum source at size scales of ∼12 AU (J. J. Tobin 2013, private communication), suggesting that L1157-mm is most likely a single source. Perhaps cores with a single system are more likely to yield an hourglass detection and/or an hourglass axis aligned with the outflow.

We thank Katherine Rosenfeld, Che-Yu Chen, and Aaron Juarez for their help in providing CARMA summer school tracks.

Support for CARMA construction was derived from the states of California, Illinois, and Maryland, the James S. McDonnell Foundation, the Gordon and Betty Moore Foundation, the Kenneth T. and Eileen L. Norris Foundation, the University of Chicago, the Associates of the California Institute of Technology, and the National Science Foundation. Ongoing CARMA development and operations are supported by the National Science Foundation under a cooperative agreement (NSF AST 08-38226) and by the CARMA partner universities.

The Caltech Submillimeter Observatory is operated by the California Institute of Technology under cooperative agreement with the National Science Foundation (AST-0838261),

and SHARP is supported by NSF grant AST-090930 to Northwestern University.

REFERENCES

Allen, A., Li, Z.-Y., & Shu, F. H. 2003, ApJ, 599, 363
Attard, M., Houde, M., Novak, G., et al. 2009, ApJ, 702, 1584
Bachiller, R., Pérez Gutiérrez, M., Kumar, M. S. N., & Tafalla, M. 2001, A&A, 372, 899
Blake, G. A., Sandell, G., van Dishoeck, E. F., et al. 1995, ApJ, 441, 689
Chandrasekhar, S., & Fermi, E. 1953, ApJ, 118, 113
Chapman, N L., Davidson, J. A., Goldsmith, P F., et al. 2013, ApJ, in press
Chiang, H.-F., Looney, L. W., & Tobin, J. J. 2012, ApJ, 756, 168
Chiang, H.-F., Looney, L. W., Tobin, J. J., & Hartmann, L. 2010, ApJ, 709, 470
Choi, M. 2005, ApJ, 630, 976
Crutcher, R. M. 1999, ApJ, 520, 706
Crutcher, R. M. 2012, ARA&A, 50, 29
Dotson, J. L., Vaillancourt, J. E., Kirby, L., et al. 2010, ApJS, 186, 406
Fiedler, R. A., & Mouschovias, T. C. 1993, ApJ, 415, 680
Galli, D., & Shu, F. H. 1993, ApJ, 417, 243
Girart, J. M., Beltrán, M. T., Zhang, Q., Rao, R., & Estalella, R. 2009, Sci, 324, 1408
Girart, J. M., Crutcher, R. M., & Rao, R. 1999, ApJL, 525, L109
Girart, J. M., Rao, R., & Marrone, D. P. 2006, Sci, 313, 812
Hildebrand, R. H. 1988, ApL&C, 26, 263
Hull, C. L. H., Plambeck, R. L., Bolatto, A. D., et al. 2013, ApJ, 768, 159
Koch, P. M., Tang, Y.-W., & Ho, P. T. P. 2012, ApJ, 747, 79
Kun, M. 1998, ApJS, 115, 59
Kwon, W., Looney, L. W., Crutcher, R. M., & Kirk, J. M. 2006, ApJ, 653, 1358
Lazarian, A. 2007, JQSRT, 106, 225
Li, H., Dowell, C. D., Kirby, L., Novak, G., & Vaillancourt, J. E. 2008, ApOpt, 47, 422
Loinard, L. 2013, in IAU Symp. 289, Advancing the Physics of Cosmic Distances, ed. R. de Gris & G. Bono (Cambridge: Cambridge Univ. Press), 36
Looney, L. W., Tobin, J. J., & Kwon, W. 2007, ApJL, 670, L131
Matthews, B. C., McPhee, C. A., Fissel, L. M., & Curran, R. L. 2009, ApJS, 182, 143
Ossenkopf, V., & Henning, T. 1994, A&A, 291, 943
Ostriker, E. C., Stone, J. M., & Gammie, C. F. 2001, ApJ, 546, 980
Rao, R., Girart, J. M., Marrone, D. P., Lai, S.-P., & Schnee, S. 2009, ApJ, 707, 921
Schleuning, D. A. 1998, ApJ, 493, 811
Tang, Y.-W., Ho, P. T. P., Koch, P. M., & Rao, R. 2010, ApJ, 717, 1262
Tang, Y.-W., Ho, P. T. P., Koch, P. M., et al. 2009, ApJ, 700, 251
Tobin, J. J., Bergin, E. A., Hartmann, L., et al. 2013, ApJ, 765, 18
Tobin, J. J., Hartmann, L., Chiang, H.-F., et al. 2012, Natur, 492, 83
Vaillancourt, J. E. 2006, PASP, 118, 1340
Vaillancourt, J. E., & Matthews, B. C. 2012, ApJS, 201, 13